PHYSICAL REVIEW LETTERS **135,** 256201 (2025)

Surface-State Engineering for Generation of Nonlinear Charge and Spin Photocurrents

Javier Sivianes,[1] Peio Garcia-Goiricelaya,[2] Daniel Hernangómez-Pérez,[3] and Julen Ibañez-Azpiroz[1,4,5]
[1]*Centro de Física de Materiales (CSIC-UPV/EHU), 20018, Donostia-San Sebastián, Spain*
[2]*Department of Physics, University of the Basque Country UPV/EHU, 48940 Leioa, Basque Country, Spain*
[3]*CIC nanoGUNE BRTA, Tolosa Hiribidea 76, 20018 San Sebastián, Spain*
[4]*IKERBASQUE, Basque Foundation for Science, 48009 Bilbao, Spain*
[5]*Donostia International Physics Center (DIPC), 20018 Donostia-San Sebastián, Spain*

(Received 7 May 2025; revised 26 September 2025; accepted 13 November 2025; published 18 December 2025)

We systematically explore the generation of nonlinear charge and spin photocurrents using spin-orbit split surface states. This mechanism enables net DC flow along the surface plane even in centrosymmetric bulk environments like the Rashba prototype Au(111), where we characterize the main quadratic contributions by combining model predictions with density functional calculations. We further identify the Tl/Si(111) surface as a prime scenario for experimental verification; with slight doping, it develops metallic surface states featuring remarkable relativistic properties deviating from the Rashba paradigm, while the bulk remains semiconducting. Its nonlinear charge photocurrent reveals a distinct angular signature and a magnitude comparable to bulk ferroelectrics, highlighting the potential of surface-state photocurrents for low-bias optoelectronic applications. Moreover, the nontrivial spin texture of its surface states enables the generation of pure out-of-plane spin-polarized currents, offering a highly versatile nonlinear spin-filtering functionality beyond the conventional spin Hall effect.

DOI: 10.1103/h8rp-rtn8

Materials that lack a center of inversion in their crystalline structure exhibit a distinctive optical effect known as the bulk photovoltaic effect (BPVE) [1–3]. This phenomenon is described by a quadratic optical response that generates a net DC photocurrent in homogeneous materials. The effect has obvious potential for applications in interface-free solar cell technologies, which represents a notable advantage over the standard photovoltaics based on pn junctions. In recent years, materials such as Weyl semimetals [4,5] or transition-metal dichalcogenide nanotubes [6,7] have exhibited a striking enhancement of the BPVE, approaching competitive figures of merit. In addition, recent works suggest that the spin-dependent counterpart of the effect [8] might pave the way for novel applications, e.g., as pure spin current generators [9] or as a knob of unconventional magnetic phases [10,11].

A significant challenge in identifying materials with an enhanced BPVE is the necessity of broken inversion symmetry, which greatly limits the pool of viable candidates. However, even in bulk centrosymmetric materials inversion symmetry is inherently broken at their *surface*, enabling symmetry-allowed quadratic optical responses [12,13]. In this scenario, the nonlinear response is expected to be most prominent in states highly localized around the surface, particularly in electronic transitions involving *surface states*. Shift and ballistic currents in topological surface states have been explored based on the Rashba model [14,15], as well as quadratic photocurrents in metallic surface alloys using a nonequilibrium Keldysh approach [16,17], including recent work on orbital contributions [18]. Additionally, the BPVE from surface Fermi arcs in Weyl semimetals has been investigated [19–21]. With their promising potential for harnessing spin-orbit physics through nonlinear charge and spin responses, surface-state photocurrents remain an open field for exploration.

In this Letter, we carry out a quantitative study of nonlinear photocurrents generated by spin-orbit split surface states. We substantiate our findings through density functional theory (DFT) calculations, offering realistic estimates for spin and charge photocurrent magnitudes in specific materials. First, we validate the fundamental principles governing the major quadratic contributions in the Au(111) surface, which features the prototype Rashba spin-orbit split states [22]. Next, we identify Tl/Si(111) as an ideal candidate for experimental realization, providing clear and measurable signatures of surface-state charge photocurrents upon doping. Finally, we show that the distinctive spin-polarization structure of its surface states near the $\bar{\mathrm{K}}$ and $\bar{\mathrm{K}}'$ valleys endows the system with a remarkable spin-filtering capability.

We begin by describing the quadratic optical contributions to the BPVE. Under a monochromatic light field $\boldsymbol{E}(t) = \boldsymbol{E}(\omega)e^{i\omega t} + \boldsymbol{E}(-\omega)e^{-i\omega t}$, the generated DC charge photocurrent ($\omega = 0$) has two sources, namely, the shift and injection currents. In a time-reversal invariant material, it can be written as

$$J^a(0) = \sigma^{abc}\mathrm{Re}[E^b(\omega)E^c(-\omega)] + \tau \cdot \eta^{abc}\,\mathrm{Im}[E^b(\omega)E^c(-\omega)] \tag{1}$$

with a, b, and c Cartesian indexes. In Eq. (1), σ^{abc} and η^{abc} stand for the shift and injection photoconductivities, respectively. The former describes an intrinsic contribution to the current originating from real-space shifts undergone by electrons upon photoexcitation, which is symmetric in the electric field indexes. In contrast, η^{abc} is antisymmetric in bc, and its generation rate is proportional to the electronic relaxation time τ. These contributions were intensively studied a few decades ago [1–3], and their modern length-gauge expressions employed in this Letter were derived in Ref. [23] (see more details in Supplemental Material (SM) [24]).

As a specific material realization, we first consider Au(111), a system where Lashell *et al.* famously reported evidence of spin-split-surface states driven by spin-orbit coupling [26]. Since then, it has become a paradigmatic example of the Rashba two-dimensional electron gas [22,27,28]. Unlike bulk Au, Au(111) belongs to the noncentrosymmetric point group $3m$, enabling symmetry-allowed quadratic optical responses at the surface. Table I displays the permitted (independent) components which can generate current under linearly polarized light and circularly polarized light by the shift and injection mechanisms, respectively.

We focus on excitations that connect the spin-orbit-split surface states of Au(111) and employ the Rashba model to gain insight into the underlying physical properties. At linear order in the crystal momentum $\mathbf{k}$, the Rashba model is isotropic. However, it can be extended with higher-order terms that comply with specific point group symmetries. In this Letter, we incorporate terms up to third order in $\mathbf{k}$ that transform according to the noncentrosymmetric point group $3m$ of Au(111), as originally proposed in Ref. [29]. The $k \cdot p$ Hamiltonian in polar coordinates (ρ, ϕ) reads

$$H = \frac{\rho^2}{2m}\mathcal{I} - (\alpha + \gamma\rho^2)\rho\sin(\phi)\sigma_x + (\alpha + \gamma\rho^2)\rho\cos(\phi)\sigma_y + \beta\rho^3\cos(3\phi)\sigma_z. \quad (2)$$

It is composed by the isotropic linear term characterized by the Rashba coupling constant α, a third order isotropic correction with coefficient γ, and the hexagonal warping term characterized by β [29]. The inclusion of hexagonal warping is essential to break the symmetry of the otherwise isotropic low energy Hamiltonian, allowing in-plane surface currents. Since for Au(111) the Rashba model is only valid in a small region close to the $\bar{\Gamma}$ point, we treat $\mathcal{O}(\rho^3)$ terms as a perturbation. The transition matrix elements of the shift and injection photocurrents can be readily calculated (see Ref. [24] for details and the rest of components):

$$\sigma^{yyy}(\mathbf{k}) = \frac{3\beta\cos^2(\phi)}{\alpha\rho}, \quad (3)$$

$$\eta^{xxy}(\mathbf{k}) = \frac{-2\alpha\beta\cos\phi\cos 3\phi}{4\rho^2(\alpha^2 + 4\alpha\gamma\rho^2)}. \quad (4)$$

Note that only $\sigma^{yyy} = -\sigma^{yxx}$ produces a finite response whereas the rest integrate to zero in $\mathbf{k}$ space, in accordance with Table I (tensor components containing z are not described by the model). Besides predicting a simple polar distribution for all contributions, Eqs. (3) and (4) clearly highlight the importance of the warping term β for a finite quadratic response, in line with Refs. [14,15].

TABLE I. Independent components of the integrated charge (abc) and spin (s, abc) shift and injection photoconductivity tensors under linearly (LPL) and circularly (CPL) polarized light that contribute to in-plane photocurrents for the $3m$ point group describing Au(111) and Tl/Si(111) surfaces.

	LPL	CPL
Charge shift	yyy, xxz	⋯
Charge injection	⋯	xxz
Spin shift	⋯	$x, xxy; x, xxz; z, xyz$
Spin injection	$x, xxy; x, xxz; x, yyy$ $x, yzz; z, xxx; z, xyz$	⋯

We now evaluate the accuracy of the model predictions by comparing them with quantitative results. This is a necessary step for establishing the foundation of surface-state photocurrent engineering using the Rashba Hamiltonian [14–16], as nonlinear responses are particularly sensitive to the approximations employed in simplified models [30,31] which can therefore miss important features [32,33]. To this end, we have performed fully relativistic DFT calculations for Au(111) using the Quantum ESPRESSO package [34,35] and computed the nonlinear optical properties by means of a Wannier interpolation technique [30,36] (see End Matter for details). Figure 1 presents a $\mathbf{k}$-resolved map of the calculated transition probabilities around $\bar{\Gamma}$, along with the Rashba model predictions overlaid for comparison. In the case of injection [Figs. 1(a) and 1(b)], the *ab initio* results match remarkably well the model predictions, both in the multilobe pattern form as well as in the sign. In comparison, the Rashba model performs worse in the qualitative description of the shift photocurrent, as evidenced by Figs. 1(c) and 1(d). This difference is likely due to the sensitivity of the shift mechanism to the quantum-geometric properties of the Bloch wave function entering in the expression of σ^{abc} [23], which are not captured completely in two-band models [32,33]. Overall, we nonetheless conclude that the Rashba model provides a reasonable description of shift and injection photoconductivities, supporting its use in future studies.

Our results for Au(111) highlight the internal structure of the main quadratic photoresponses driven by Rashba surface states, and open up the possibility of extracting the hexagonal warping constant β through optical

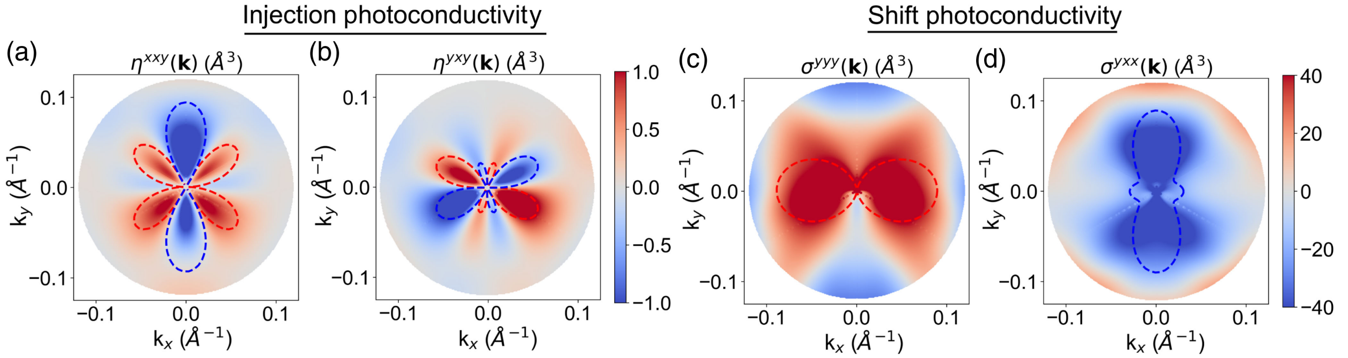

FIG. 1. Components of **k**-resolved transition matrix elements of the injection (a), (b) and shift (c), (d) photoconductivities, showing with a color map the values calculated by DFT for the Au(111) surface states. The dashed lines represent contour lines of constant values from the analytical calculations based on the Rashba model [Eqs. (3) and (4) correspond to (c) and (a), respectively].

measurements of the symmetry-allowed shift component σ^{yyy}. However, the metallic nature of bulk Au states might present a practical challenge for such purpose due to hybridization with the surface Rashba bands. Consequently, we now shift our focus to the Tl/Si(111) surface, whose electronic properties are also prominently influenced by the spin-orbit interaction and possesses important advantages over Au(111). First, due to the material's semiconducting nature, the surface response remains well isolated and distinguishable from any bulk current contribution [37,38]. Second, it hosts a pair of unoccupied spin-split surface states, as shown in Fig 2, which can be accessed by inverse photoemission spectroscopy at $\bar{\mathrm{K}}$, $\bar{\mathrm{K}}'$ valleys [39,40]. Third, these surface states exhibit a huge spin-orbit splitting of ∼0.6 eV—a value well-suited for optical applications—accompanied by an out-of-plane spin polarization at the $\bar{\mathrm{K}}$ and $\bar{\mathrm{K}}'$ valleys, completely deviating from the Rashba model predictions [41,42].

We have performed *ab initio* calculations for the Tl/Si(111) surface following the same procedure as described earlier for Au(111) (see End Matter). As Tl/Si(111) belongs to the $3m$ point group, the allowed photoconductivity components are those contained in Table I. We therefore focus on the symmetry-allowed shift component σ^{yyy} associated with transitions between the spin-orbit split surface states indicated in Fig. 2(a), where the lowest band can be populated by electron doping.

The inset in Fig. 2(b) shows that for a moderate doping level of $\mu = 0.3$ eV, the shift photoconductivity is largest around $\omega \simeq 0.6$ eV, with maximum $|\sigma^{yyy}| \simeq 2\ \mu\mathrm{A/V}^2$. Notably, the surface-state photoconductivity translates into a measurable in-plane photocurrent. This is proven in main Fig. 2(b), where we illustrate how the maximum of the photocurrent-to-power ratio J^y/P behaves as a function of doping. At doping levels ranging from 0 to ∼0.6 eV, we observe that the nonlinear shift photocurrent flowing along the surface plane is substantial, comparable or even larger than values reported in prototypic bulk materials like $\mathrm{BaTiO_3}$ [43], $\mathrm{BiFeO_3}$ [44], and other semiconductors [45–49]. This prediction regarding the magnitude of surface-state shift photocurrents is a central result of this Letter, as it incorporates critical factors such as reflection and absorption via the Glass coefficient [50]. These elements are essential for a realistic estimation of nonlinear optical processes [49]; technical details are provided in the End Matter.

In addition to the magnitude, in Fig. 2(c) we analyze the angular dependence of the photocurrent as a function of the light polarization in the xy plane. We find that the shift current is maximized along the crystallographic x and y axes, whereas it vanishes at $45 + n \cdot 90$ deg angles for integer n. This provides a clear signature for experimental detection of a surface-state nonlinear DC charge photocurrent. A separate DC component could also arise from the conventional photovoltaic effect, in which a photon is absorbed and then driven by the effective electrostatic field near the surface, $E_z(0)$. Such photoexcitation would be described by the linear absorption with an angular dependence different from the shift current [see Fig. 2(c) and [24]], making it straightforward to distinguish, for example, by measuring along $\theta = 0$. Moreover, because the electrostatic field is expected to mainly point perpendicular to the surface, this mechanism is unlikely to generate a significant in-plane photocurrent. Nonlinear ballistic currents arising from asymmetric processes such as electron-phonon scattering might also contribute to the DC photocurrent with their own angular pattern [15]. While they can, in some cases, reach magnitudes comparable to the shift current [51,52], the electron–phonon coupling in the unoccupied surface states of Tl/Si(111) is particularly weak due to spin-locked intervalley scattering between $\bar{\mathrm{K}}$ and $\bar{\mathrm{K}}'$ [53]. As a consequence, we expect the angular dependence of the DC photocurrent to be predominantly governed by the shift-current pattern shown in Fig. 2(c).

In the remaining part of the Letter, we extend our analysis to the spin contribution to the BPVE. Nonlinear spin photocurrents have received significantly less attention

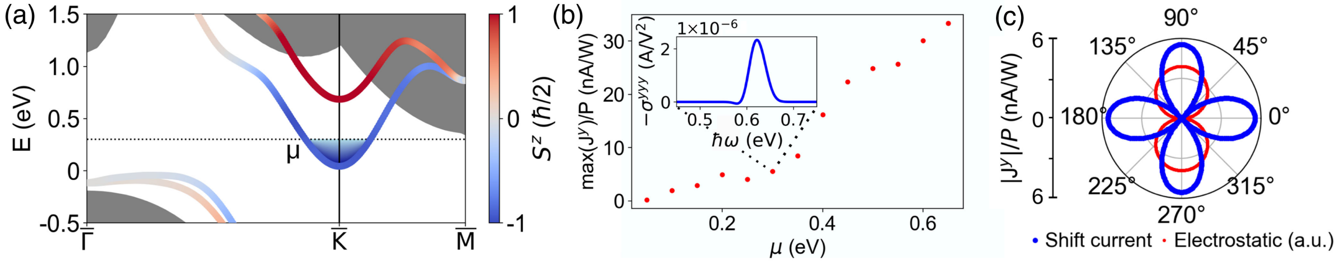

FIG. 2. (a) Band structure of Tl/Si(111) showing the out-of-plane spin polarization of the surface bands (given by the color code). The dotted line represents the chemical potential, μ, for a n-doped system. (b) Maximum value of the shift current as a function of doping. At each value of μ, the frequency and polarization of the light is chosen to maximize the current. The inset shows the 3D shift photoconductivity spectra for $\mu = 0.3$ eV. (c) In blue, angular distribution of the shift current generated by linearly polarized light with varying polarization angle θ and frequency $\omega = 0.63$ eV for $\mu = 0.3$ eV. In red, the pattern of the possible electrostatic contribution (arbitrary units).

than the charge counterparts, with notable progress emerging only recently [8,14,54]. While most studies have so far focused on bulk spin currents [9,55,56], the surface states of heavy-element materials provide an ideal setting to explore the interplay between spin-orbit interaction and various nonlinear spin contributions [14,16,17]. In this Letter, we have adopted the formalism established by Lihm and Park [8], where transition matrix elements associated to the spin shift and injection currents are expressed in the length gauge and are therefore naturally suited for Wannier interpolation techniques (see Ref. [24]). In analogy with Eq. (1), in a time-reversal invariant material, one can write the quadratic spin current density $J^{s,a}$ as (s represents spin projection)

$$J^{s,a}(0) = \tau \cdot \xi^{s,abc}\mathrm{Re}[E^b(\omega)E^c(-\omega)] + \zeta^{s,abc}\,\mathrm{Im}[E^b(\omega)E^c(-\omega)], \tag{5}$$

where $\xi^{s,abc}$ and $\zeta^{s,abc}$ are the spin injection and shift photoconductivities, respectively.

Table I lists the symmetry-allowed spin shift and injection tensor components for Au(111) and Tl/Si(111). As sketched in Fig. 3(a), these mechanism provide a remarkable spin-filtering functionality; they can generate a DC spin current that is spin polarized along the out-of-plane or in-plane directions depending on the polarization of light. From the standpoint of symmetry alone, both surfaces should exhibit this functionality. In practice, however, our DFT calculations show that Au(111) generates negligible out-of-plane spin current, which is a direct consequence of the purely in-plane spin texture of its surface states (see SM [24]). Therefore, we focus our subsequent analysis on Tl/Si(111).

Let us begin by inspecting the **k**-space distribution of the nonlinear spin photoconductivity. In Fig. 3(b) we present the **k**-resolved contributions for both in-plane and out-of-plane spin injection components, symmetrized to preserve the relevant crystal symmetries (see End Matter). Overall, they share the same order of magnitude but are distributed differently across the BZ. The dominant out-of-plane contribution arises through the component $\xi^{z,xxx}$, whereas the largest in-plane component is $\xi^{x,yyy}$. Their calculated spectra is displayed in Fig. 3(c) for two representative values of the chemical potential, $\mu = 0.25$ and $\mu = 0.45$ eV. Notably, at $\mu = 0.25$ eV the spin injection is predominantly governed by the out-of-plane component, whereas at $\mu = 0.45$ eV, the in-plane contribution becomes quantitatively relevant. Thus, in practice, Tl/Si(111) acts as a spin injector or filter as a function of doping and light polarization, generating spin-polarized currents with a well-defined out-of-plane spin component S_z for $\mu \sim 0.25$ eV and x-polarized light.

In order to understand the origin of these results, in Fig. 3(d) we display the **k**-resolved structure of several relevant quantities along the high-symmetry path $\bar{K} - \bar{\Gamma}$, where we mark the Fermi surface cuts for the two doping levels $\mu = 0.25$ and 0.45 eV. We start by examining the top panel, which shows the velocity matrix elements Δv^x and Δv^y that contribute to the $\xi^{z,xxx}$ and $\xi^{x,yyy}$ components, respectively (see Ref. [24]). Since both surface states exhibit a band minimum at $\bar{K}$ [see Fig. 2(a)], the velocity remains very small near this valley (the same happens at $\bar{K}'$). As a result, the two components shown in the middle panel of Fig. 3(d) are also very small in the close vicinity of the valley, with both peaking away from $\bar{K}$. The origin of the strong peak in $\xi^{z,xxx}$ can be traced back to the out-of-plane spin-polarization of surface states, illustrated in the lower panel of Fig. 3(d). A comparison with the middle panel reveals that $\xi^{z,xxx}$ peaks in the region where S_z dominates, whereas $\xi^{x,yyy}$ peaks only when S_z becomes significantly smaller. This highlights the crucial role of the out-of-plane spin polarization—completely absent in Au(111)—in generating a nonlinear spin current perpendicular to the plane in Tl/Si(111).

To conclude our analysis, we note that the nonlinear spin accumulation generated by the mechanism described above should be detectable using magneto-optical techniques based on ultrafast laser pulses such as Kerr

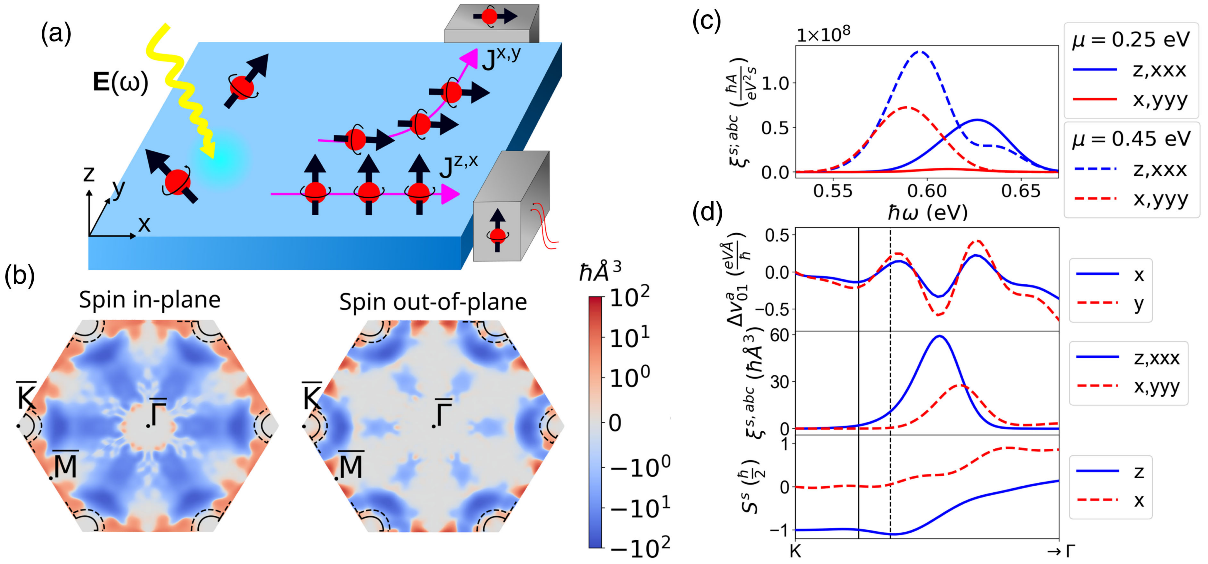

FIG. 3. (a) Schematic representation of nonlinear spin current generation by surface states. Out-of-plane ($\hat{\mathbf{z}}$) or in-plane ($\hat{\mathbf{x}}$) spin DC currents can be directed to different contacts at the surface depending on the polarization of the incident light field. (b) Brillouin zone $\mathbf{k}$-resolved spin out-of-plane (top) and in-plane (bottom) combinations of the spin injection conductivity tensor components. The continuous and dashed arcs around the valleys denote the projected Fermi surfaces at $\mu = 0.25$ eV and $\mu = 0.45$ eV, respectively. (c) Spectra of $\xi^{z,xxx}$ and $\xi^{x,yyy}$ for $\mu = 0.25$ eV and $\mu = 0.45$ eV. Note that at $\mu = 0.25$ eV only the out-of-plane component contributes significantly. (d) $\mathbf{k}$-resolved quantities along the $\bar{\mathrm{K}} - \bar{\Gamma}$ path, where the vertical solid and dashed lines correspond to the intersection of the path with the Fermi surfaces illustrated in (b). Top: variation in the difference of the intraband velocity along $a = x$. Middle: $\xi^{z,xxx}$ and $\xi^{y,xxx}$ components polarized out of plane ($\hat{\mathbf{z}}$, blue curve) and in plane ($\hat{\mathbf{x}}$, red curve). Bottom: out-of-plane and in-plane spin polarization components.

microscopy [57,58]. Alternatively, the associated spin transport phenomena could be probed via the inverse spin Hall effect [59,60]. This is particularly promising, as it would enable an optically controlled, on-demand nonlinear spin filter and injector, without the need for ferroelectric materials [61] or bulk crystals with purely in-plane spin textures [62].

In summary, we have presented a detailed study of nonlinear photocurrents arising from spin-orbit split surface states. Besides validating the fundamental aspects of the effect in the Rashba prototype Au(111) surface, we have identified an optimal platform for experimental detection in the Tl/Si(111) surface. Our calculations have shown that the magnitude of the generated bulk photovoltaic effect is well within the measurable limits, and we have provided clear angular fingerprints for its detection. While we have focused on Tl/Si(111), the effect is general given that it does not require inversion-symmetry breaking of the bulk substrate, hence similar features should be expected in other extensively studied heavy-element compounds [63–67]. Additionally, we have explored the nonlinear spin counterpart of this effect, demonstrating that Tl/Si(111) functions as an effective spin filter, with its performance tunable through doping. Notably, nonlinear spin currents provide far greater flexibility than the conventional linear approach, which is limited by the lower dimensionality of the spin Hall conductivity tensor and only permits transverse spin accumulation [57,68,69]. The interplay between spin texture and nonlinear responses paves the way for novel strategies in engineering spatial- and spin-selective nonlinear spin generation, offering enhanced control and tunability for spintronic applications.

Acknowledgments—The authors thank F. de Juan for insightful discussions and highlighting relevant literature. J. S., P. G.-G., and J. I.-A. acknowledge the financial support of the European Union's Horizon 2020 research and innovation program under the European Research Council (ERC) Grant Agreement No. 946629 StG PhotoNow. D. H.-P. is grateful for funding from the Diputación Foral de Gipuzkoa through Grants No. 2023-FELL-000002-01, No. 2024-FELL-000009-01, No. 2025-FELL-000004-01 and No. 2025-CIE4-000036-01. D. H.-P. and J. I.-A. are also grateful from support of the Spanish MICIU/AEI /10.13039/501100011033 and FEDER, UE through Project No. PID2023-147324NA-I00. The authors acknowledge support from IKUR Strategy, Quantum Technologies 2025 project M-Twist, from the Department of Science, Universities and Innovation of the Basque Government.

Data availability—The data that support the findings of this Letter are openly available [70].

[1] V. I. Belinicher, E. L. Ivchenko, and B. I. Sturman, Kinetic theory of the displacement photovoltaic effect in piezoelectrics, Zh. Eksp. Teor. Fiz. **83**, 649 (1982).

[2] B. I. Sturman and V. M. Fridkin, *The photovoltaic and photorefractive effects in noncentrosymmetric materials* (Gordon and Breach, London, 1992).

[3] R. von Baltz and W. Kraut, Theory of the bulk photovoltaic effect in pure crystals, Phys. Rev. B **23**, 5590 (1981).

[4] J. Ma, Q. Gu, Y. Liu, J. Lai, P. Yu, X. Zhuo, Z. Liu, J.-H. Chen, J. Feng, and D. Sun, Nonlinear photoresponse of type-II Weyl semimetals, Nat. Mater. **18**, 476 (2019).

[5] G. B. Osterhoudt, L. K. Diebel, M. J. Gray, X. Yang, J. Stanco, X. Huang, B. Shen, N. Ni, P. J. Moll, Y. Ran *et al.*, Colossal mid-infrared bulk photovoltaic effect in a type-I Weyl semimetal, Nat. Mater. **18**, 471 (2019).

[6] Y. J. Zhang, T. Ideue, M. Onga, F. Qin, R. Suzuki, A. Zak, R. Tenne, J. H. Smet, and Y. Iwasa, Enhanced intrinsic photovoltaic effect in tungsten disulfide nanotubes, Nature (London) **570**, 349 (2019).

[7] J. Krishna, P. Garcia-Goiricelaya, F. de Juan, and J. Ibañez-Azpiroz, Understanding the large shift photocurrent of WS_2 nanotubes: A comparative analysis with monolayers, Phys. Rev. B **108**, 165418 (2023).

[8] J.-M. Lihm and C.-H. Park, Comprehensive theory of second-order spin photocurrents, Phys. Rev. B **105**, 045201 (2022).

[9] H. Xu, H. Wang, J. Zhou, and J. Li, Pure spin photocurrent in non-centrosymmetric crystals: Bulk spin photovoltaic effect, Nat. Commun. **12**, 4330 (2021).

[10] R. Dong, R. Cao, D. Tan, and R. Fei, Crystal symmetry selected pure spin photocurrent in altermagnetic insulators, arXiv:2412.09216.

[11] J. Sivianes, F. J. Santos, and J. Ibañez-Azpiroz, Optical signatures of spin symmetries in unconventional magnets, Phys. Rev. Lett. **134**, 196907 (2025).

[12] N. Arzate, R. A. Vázquez-Nava, and Bernardo S. Mendoza, Optical spin- and current-injection study on Si(111)-In surfaces, Phys. Rev. B **90**, 205310 (2014).

[13] J. L. Cabellos, Bernardo S. Mendoza, and A. I. Shkrebtii, Optical coherent current control at surfaces: Theory of injection current, Phys. Rev. B **84**, 195326 (2011).

[14] K. W. Kim, T. Morimoto, and N. Nagaosa, Shift charge and spin photocurrents in Dirac surface states of topological insulator, Phys. Rev. B **95**, 035134 (2017).

[15] N. V. Leppenen and L. E. Golub, Linear photogalvanic effect in surface states of topological insulators, Phys. Rev. B **107**, L161403 (2023).

[16] F. Freimuth, S. Blügel, and Y. Mokrousov, Charge and spin photocurrents in the Rashba model, Phys. Rev. B **103**, 075428 (2021).

[17] T. Adamantopoulos, M. Merte, D. Go, F. Freimuth, S. Blügel, and Y. Mokrousov, Laser-induced charge and spin photocurrents at the $BiAg_2$ surface: A first-principles benchmark, Phys. Rev. Res. **4**, 043046 (2022).

[18] T. Adamantopoulos, M. Merte, D. Go, F. Freimuth, S. Blügel, and Y. Mokrousov, Orbital Rashba effect as a platform for robust orbital photocurrents, Phys. Rev. Lett. **132**, 076901 (2024).

[19] G. Chang, J.-X. Yin, T. Neupert, Daniel S. Sanchez, I. Belopolski, Songtian S. Zhang, Tyler A. Cochran, Z. Chéng, M.-C. Hsu, S.-M. Huang, B. Lian, S.-Y. Xu, H. Lin, and M. Z. Hasan, Unconventional photocurrents from surface Fermi arcs in topological chiral semimetals, Phys. Rev. Lett. **124**, 166404 (2020).

[20] J. Cao, M. Wang, Z.-M. Yu, and Y. Yao, Bulk fermi arc transition induced large photogalvanic effect in Weyl semimetals, Phys. Rev. B **106**, 125416 (2022).

[21] J. F. Steiner, A. V. Andreev, and M. Breitkreiz, Surface photogalvanic effect in Weyl semimetals, Phys. Rev. Res. **4**, 023021 (2022).

[22] J. Henk, M. Hoesch, J. Osterwalder, A. Ernst, and P. Bruno, Spin-orbit coupling in the L-gap surface states of Au(111): spin-resolved photoemission experiments and first-principles calculationsJ. Phys. Condens. Matter **16**, 7581 (2004).

[23] J. E. Sipe and A. I. Shkrebtii, Second-order optical response in semiconductors, Phys. Rev. B **61**, 5337 (2000).

[24] See Supplemental Material at http://link.aps.org/supplemental/10.1103/h8rp-rtn8 for additional information of the charge and spin photonconductivity expression, model, and material calculations, which includes Refs. [8,23,25].

[25] S. S. Tsirkin, High performance Wannier interpolation of berry curvature and related quantities with WannierBerri code, npj Comput. Mater. **7**, 33 (2021).

[26] S. LaShell, B. A. McDougall, and E. Jensen, Spin splitting of an Au(111) surface state band observed with angle resolved photoelectron spectroscopy, Phys. Rev. Lett. **77**, 3419 (1996).

[27] M. Heide, G. Bihlmayer, P. Mavropoulos, A. Bringer, and S. Blügel, Spin orbit driven physics at surfaces, Psi-k Newsl. **78**, 1109 (2006), https://psi-k.net/download/highlights/Highlight_78.pdf.

[28] J. Ibañez-Azpiroz, A. Bergara, E. Y. Sherman, and A. Eiguren, Spin-flip transitions and departure from the Rashba model in the Au(111) surface, Phys. Rev. B **88**, 125404 (2013).

[29] L. Fu, Hexagonal warping effects in the surface states of the topological insulator Bi_2Te_3, Phys. Rev. Lett. **103**, 266801 (2009).

[30] J. Ibañez-Azpiroz, Stepan S. Tsirkin, and I. Souza, Ab initio calculation of the shift photocurrent by Wannier interpolation, Phys. Rev. B **97**, 245143 (2018).

[31] C. Wang, X. Liu, L. Kang, B.-L. Gu, Y. Xu, and W. Duan, First-principles calculation of nonlinear optical responses by Wannier interpolation, Phys. Rev. B **96**, 115147 (2017).

[32] J. Ibañez-Azpiroz, F. de Juan, and I. Souza, Assessing the role of interatomic position matrix elements in tight-binding calculations of optical properties, SciPost Phys. **12**, 070 (2022).

[33] A. Ghosh, Aaron M. Schankler, and Andrew M. Rappe, Choosing tight-binding models for accurate optoelectronic responses, Phys. Rev. B **111**, 125203 (2025).

[34] P. Giannozzi *et al.*, QUANTUM ESPRESSO: A modular and open-source software project for quantum simulations of materials, J. Phys. Condens. Matter **21**, 395502 (2009).

[35] P. Giannozzi *et al.*, Advanced capabilities for materials modelling with Quantum ESPRESSO, J. Phys. Condens. Matter **29**, 465901 (2017).

[36] A. R. Puente-Uriona, S. S. Tsirkin, I. Souza, and J. Ibañez-Azpiroz, Ab initio study of the nonlinear optical properties

and dc photocurrent of the Weyl semimetal $TaIrTe_4$, Phys. Rev. B **107**, 205204 (2023).

[37] K. Sakamoto, T. Oda, A. Kimura, K. Miyamoto, M. Tsujikawa, A. Imai, N. Ueno, H. Namatame, M. Taniguchi, P. E. J. Eriksson, and R. I. G. Uhrberg, Abrupt rotation of the Rashba spin to the direction perpendicular to the surface, Phys. Rev. Lett. **102**, 096805 (2009).

[38] K. Sakamoto, T.-H. Kim, T. Kuzumaki, B. Müller, Y. Yamamoto, M. Ohtaka, J. R. Osiecki, K. Miyamoto, Y. Takeichi, A. Harasawa, S. D. Stolwijk, A. B. Schmidt, J. Fujii, R. I. G. Uhrberg, M. Donath, H. W. Yeom, and T. Oda, Valley spin polarization by using the extraordinary Rashba effect on silicon, Nat. Commun. **4**, 2073 (2013).

[39] S. D. Stolwijk, A. B. Schmidt, M. Donath, K. Sakamoto, and P. Krüger, Rotating spin and giant splitting: Unoccupied surface electronic structure of Tl/Si(111), Phys. Rev. Lett. **111**, 176402 (2013).

[40] S. D. Stolwijk, A. B. Schmidt, K. Sakamoto, P. Krüger, and M. Donath, Valley spin polarization of Tl/Si(111), Phys. Rev. Mater. **1**, 064604 (2017).

[41] M.-H. Liu and C.-R. Chang, Upstanding Rashba spin in honeycomb lattices: Electrically reversible surface spin polarization, Phys. Rev. B **80**, 241304(R) (2009).

[42] J. Ibañez-Azpiroz, A. Eiguren, and A. Bergara, Relativistic effects and fully spin-polarized Fermi surface at the Tl/Si(111) surface, Phys. Rev. B **84**, 125435 (2011).

[43] W. T. H. Koch, R. Munser, and P. Würfel, Anomalous photovoltage in $BaTiO_3$, Ferroelectrics **13**, 305 (1976).

[44] S. M. Young, F. Zheng, and A. M. Rappe, First-principles calculation of the bulk photovoltaic effect in bismuth ferrite, Phys. Rev. Lett. **109**, 236601 (2012).

[45] S. M. Young and A. M. Rappe, First principles calculation of the shift current photovoltaic effect in ferroelectrics, Phys. Rev. Lett. **109**, 116601 (2012).

[46] S. Y. Yang, J. Seidel, S. J. Byrnes, P. Shafer, C.-H. Yang, M. D. Rossell, P. Yu, Y.-H. Chu, J. F. Scott, J. W. Ager III, L. W. Martin, and R. Ramesh, Above-bandgap voltages from ferroelectric photovoltaic devices, Nat. Nanotechnol. **5**, 143 (2010).

[47] J. Ibañez-Azpiroz, I. Souza, and F. de Juan, Directional shift current in mirror-symmetric BC_2N, Phys. Rev. Res. **2**, 013263 (2020).

[48] F. Delodovici and C. Paillard, Photogalvanic shift currents in $BiFeO_3$–$LaFeO_3$ superlattices, ACS Appl. Energy Mater. **8**, 1716 (2025).

[49] L. Z. Tan, F. Zheng, S. M. Young, F. Wang, S. Liu, and A. M. Rappe, Shift current bulk photovoltaic effect in polar materials—hybrid and oxide perovskites and beyond, npj Comput. Mater. **2**, 16026 (2016).

[50] A. M. Glass, D. von der Linde, and T. J. Negran, High-voltage bulk photovoltaic effect and the photorefractive process in $LiNbO_3$, Appl. Phys. Lett. **25**, 233 (1974).

[51] Z. Dai, Aaron M. Schankler, L. Gao, Liang Z. Tan, and A. M. Rappe, Phonon-assisted ballistic current from first-principles calculations, Phys. Rev. Lett. **126**, 177403 (2021).

[52] Z. Dai and A. M. Rappe, First-principles calculation of ballistic current from electron-hole interaction, Phys. Rev. B **104**, 235203 (2021).

[53] P. Garcia-Goiricelaya, I. G. Gurtubay, and A. Eiguren, Coupled spin and electron-phonon interaction at the Tl/Si(111) surface from relativistic first-principles calculations, Phys. Rev. B **97**, 201405(R) (2018).

[54] H. Xu, H. Wang, J. Zhou, and J. Li, Pure spin photocurrent in non-centrosymmetric crystals: Bulk spin photovoltaic effect, Nat. Commun. **12**, 4330 (2021).

[55] S. M. Young, F. Zheng, and A. M. Rappe, Prediction of a linear spin bulk photovoltaic effect in antiferromagnets, Phys. Rev. Lett. **110**, 057201 (2013).

[56] R. Fei, S. Yu, Y. Lu, L. Zhu, and L. Yang, Switchable enhanced spin photocurrent in Rashba and cubic Dresselhaus ferroelectric semiconductors, Nano Lett. **21**, 2265 (2021).

[57] Y. K. Kato, R. C. Myers, A. C. Gossard, and D. D. Awschalom, Observation of the spin Hall effect in semiconductors, Science **306**, 1910 (2004).

[58] T. Ogasawara, Time-resolved vector-field imaging of spin-wave propagation in permalloy stripes using wide-field magneto-optical Kerr microscopy, Phys. Rev. Appl. **20**, 024010 (2023).

[59] E. Saitoh, M. Ueda, H. Miyajima, and G. Tatara, Conversion of spin current into charge current at room temperature: Inverse spin-Hall effect, Appl. Phys. Lett. **88**, 182509 (2006).

[60] T. Kimura, Y. Otani, T. Sato, S. Takahashi, and S. Maekawa, Room-temperature reversible spin Hall effect, Phys. Rev. Lett. **98**, 156601 (2007).

[61] X. Liu, J. D. Burton, M. Y. Zhuravlev, and Evgeny Y. Tsymbal, Electric control of spin injection into a ferroelectric semiconductor, Phys. Rev. Lett. **114**, 046601 (2015).

[62] Z. Kovács-Krausz, A. M. Hoque, P. Makk, B. Szentpéteri, M. Kocsis, B. Fülöp, M. V. Yakushev, T. V. Kuznetsova, O. E. Tereshchenko, K. A. Kokh, I. E. Lukács, T. Taniguchi, K. Watanabe, S. P. Dash, and S. Csonka, Electrically controlled spin injection from giant Rashba spin–orbit conductor BiTeBr, Nano Lett. **20**, 4782 (2020).

[63] G. Bihlmayer, P. M. Buhl, B. Dupe, I. L. Fernandes, F. Freimuth, J. Gayles, S. Heinze, N. Kiselev, S. Lounis, Y. Mokrousov, and S. Blügel, Magnetic skyrmions: Structure, stability, and transport phenomena, Psi-k Newsl.-Highlights **139**, 40 (2018), https://psi-k.net/download/highlights/Highlight_139.pdf.

[64] J. Ibañez-Azpiroz, A. Eiguren, E. Y. Sherman, and A. Bergara, Spin-flip transitions induced by time-dependent electric fields in surfaces with strong spin-orbit interaction, Phys. Rev. Lett. **109**, 156401 (2012).

[65] K. Yaji, Y. Ohtsubo, S. Hatta, H. Okuyama, K. Miyamoto, T. Okuda, A. Kimura, H. Namatame, M. Taniguchi, and T. Aruga, Large Rashba spin splitting of a metallic surface-state band on a semiconductor surface, Nat. Commun. **1**, 17 (2010).

[66] I. Gierz, T. Suzuki, E. Frantzeskakis, S. Pons, S. Ostanin, A. Ernst, J. Henk, M. Grioni, K. Kern, and C. R. Ast, Silicon surface with giant spin splitting, Phys. Rev. Lett. **103**, 046803 (2009).

[67] G. Bihlmayer, S. Blügel, and E. V. Chulkov, Enhanced Rashba spin-orbit splitting in Bi/Ag(111) and Pb/Ag(111) surface alloys from first principles, Phys. Rev. B **75**, 195414 (2007).

[68] J. Sinova, D. Culcer, Q. Niu, N. A. Sinitsyn, T. Jungwirth, and A. H. MacDonald, Universal intrinsic spin Hall effect, Phys. Rev. Lett. **92**, 126603 (2004).

[69] J. Schliemann, Spin Hall effect, Int. J. Mod. Phys. B **20**, 1015 (2006).

[70] J. Sivianes Castaño, P. Garcia-Goiricelaya, D. Hernangómez Pérez, and J. Ibañez-Azpiroz, Resources from "Surface-state engineering for nonlinear charge and spin photocurrent generation", Zenodo, Version v110.5281/zenodo.17211635 (2025).

[71] J. P. Perdew, K. Burke, and M. Ernzerhof, Generalized gradient approximation made simple, Phys. Rev. Lett. **77**, 3865 (1996).

[72] G. Pizzi *et al.*, Wannier90 as a community code: New features and applications, J. Phys. Condens. Matter **32**, 165902 (2020).

[73] H. Lee and H. J. Choi, Role of *d* orbitals in the Rashba-type spin splitting for noble-metal surfaces, Phys. Rev. B **86**, 045437 (2012).

[74] R. Fei, Liang Z. Tan, and Andrew M. Rappe, Shift-current bulk photovoltaic effect influenced by quasiparticle and exciton, Phys. Rev. B **101**, 045104 (2020).

[75] P. Garcia-Goiricelaya, J. Krishna, and J. Ibañez-Azpiroz, Including many-body effects into the wannier-interpolated quadratic photoresponse tensor, Phys. Rev. B **107**, 205101 (2023).

End Matter

Modeling Surfaces

Computational details— Density functional theory (DFT) calculations were performed using the Quantum ESPRESSO package [34,35] with the Perdew-Burke-Ernzerhof (PBE) pseudopotential [71] as an approximation for the exchange-correlation term. In the case of Au(111), the slab consisted of 7 unit cells, with an energy cutoff of 45 Ry and a Monkhorst-Pack grid of $8 \times 8 \times 1$ $\mathbf{k}$ points. For doping, we followed the standard practice of rigidly shifting the chemical potential, given that the applied shifts are restricted to a small window close the neutrality point. Maximally localized Wannier functions were then constructed from the Bloch eigenstates using the Wannier90 software package [72], where the surface states were projected onto p_z orbitals [73] (see Ref. [24] for additional parameter details and band structure). Finally, the $\mathbf{k}$-resolved shift and injection photoconductivities were computed following the methodology described in Ref. [30]. As the maximal localization process does not enforce crystal symmetries, the $\mathbf{k}$-resolved quantities were symmetrized in the following way. First, we choose an irreducible Brillouin zone. Then, the rest of the Brillouin zone is generated as $\sigma^{abc}(\mathbf{k}) = \sum_{\alpha\beta\gamma} M_{a\alpha} M_{b\beta} M_{c\gamma} \sigma^{\alpha\beta\gamma}(M^{-1}\mathbf{k})$ where M is the matrix representation of a crystal symmetry. Finally, the results from all possible choices are averaged.

For the calculations on Tl/Si(111) we proceed in the same manner as for the Au(111) surface. In this case, the simulation parameters are a slab size of 4 unit cells, an energy cutoff of 200 Ry, a $24 \times 24 \times 1$ $\mathbf{k}$-point grid, and projections with $l = 1, m_r = 1$ for the unoccupied states. For the calculation of the spectra, the WannierBerri code was employed [25]. To convert the slab-calculated photoconductivities to their 3D equivalents, a rescaling factor must be applied that accounts for the dimensions of the slab used in the surface simulations:

$$\eta_{\mathrm{3D}}^{abc} = \frac{\text{width of slab}}{\text{width of active layers}} \eta_{\mathrm{slab}}^{abc}. \tag{A1}$$

According to Ref. [12], which studies In/Si(111) surfaces, the majority of the injection photoconductivity contribution originates from the first four layers of the material. This coincides roughly with the extension of surface states reported for Tl/Si(111) [42], hence we consider a total width of active layers of $d = 6.91$ Å in Eq. (A1).

Absorption and reflection for current generation—In order to calculate the photocurrent from quadratic optical responses, the expression for a sample of thickness d illuminated by a laser with spot size of width w reads [7,74],

$$J^a = G^{abb}(\omega) \cdot (1 - R(\omega))(1 - e^{-\alpha^{bb} \cdot d}) \cdot w \cdot I^b, \tag{A2}$$

which is valid both for surfaces as well as bulk structures. Above, $I^b = c\epsilon_0 (E^b)^2/2$ is the incident light intensity for an applied electric field E^b, $R(\omega)$ the reflectivity and $\alpha^{bb}(\omega) = \sqrt{2}(\omega/c)\sqrt{|\epsilon^{bb}| - \mathrm{Re}(\epsilon^{bb})}$ which involves the dielectric function $\epsilon^{ab}(\omega)$. Finally, $G^{abb}(\omega) = 2\sigma^{abb}(\omega)/c\epsilon_0\sqrt{\epsilon_r} \cdot \alpha^{bb}(\omega)$ stands for the Glass coefficient, which quantifies the generation of photocurrents in bulk materials taking absorption into account [49,50]. In our calculations, we consider a laser spot size of 5 μm in line with Ref. [4]. Additionally, the reflectivity can be calculated as

$$R(\omega) = \left| \frac{\sqrt{\epsilon(\omega)} - 1}{\sqrt{\epsilon(\omega)} + 1} \right|^2. \tag{A3}$$

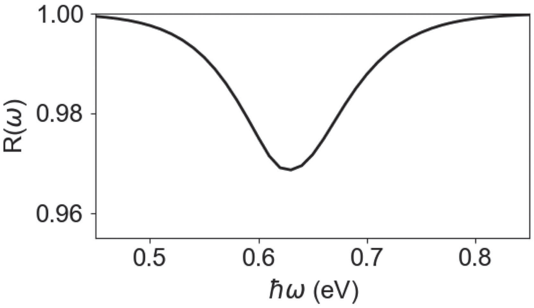

FIG. 4. Reflectivity of Tl/Si(111) for $\mu = 0.30$ eV.

As the n-doped Tl/Si(111) is metallic, the contribution to $\epsilon(\omega)$ from the Drude conductivity was included following the implementation in Ref. [75]. Figure 4 shows the frequency dependent reflectivity for $\mu = 0.3$ eV. Our calculations show that in the vicinity of the surface-state spin-splitting value of ~0.6 eV, 3% of all incoming light is absorbed by the surface states. We note that this is in line with previous estimates for spin-split surface states in [64].

Symmetric combinations of $\mathbf{k}$*-resolved spin tensor*—Figure 3 in the main text shows symmetric combinations of the $\mathbf{k}$-resolved spin injection photoconductivities

$$\Xi(\mathbf{k}) = \sum_{s,abc} C^{s,abc}\xi^{s,abc}(\mathbf{k}), \tag{A4}$$

in the sense that $\Xi(\mathbf{k}) = \Xi(M^{-1}\,\mathbf{k})$ with M a crystal symmetry. The reasoning behind this choice is to show how the spin-polarized injection current along the out-of-plane direction (z, abc components) is correlated to the spin texture which is mostly polarized along z around K in a way that it does not depend on the choice of K. As the effect of a crystal symmetry on the spin injection photoconductivity is

$$\xi^{s,abc}(\mathbf{k}) = \sum_{s'a'b'c'} M_{ss'}M_{aa'}M_{bb'}M_{cc'}\xi^{s',a'b'c'}(M^{-1}\mathbf{k}), \tag{A5}$$

then the relations

$$\Xi(\mathbf{k}) = \sum_{s,abc} C^{s,abc} \sum_{s'a'b'c'} M_{ss'}M_{aa'}M_{bb'}M_{cc'}\xi^{s',a'b'c'}(M^{-1}\mathbf{k}) \tag{A6}$$

$$\Xi(\mathbf{k}) = \Xi(M^{-1}\mathbf{k}) = \sum_{s,abc} C^{s,abc}\xi^{s,abc}(M^{-1}\mathbf{k}) \tag{A7}$$

form a system of equations which gives as a result the coefficients $C^{s,abc}$, which need not be unique.

In the case of the $3m$ point group, we find the following combinations to be invariant under C_3 rotation and M_x mirror symmetry operations, one combining tensors that are out-of-plane and one in-plane spin polarized:

$$\Xi^{\mathrm{out}}(\mathbf{k}) \propto -\xi^{z,xxx}(\mathbf{k}) + \xi^{z,xyy}(\mathbf{k}) + 2\xi^{z,yxy}(\mathbf{k}) \tag{A8}$$

$$\Xi^{\mathrm{in}}(\mathbf{k}) \propto -\xi^{x,yxx}(\mathbf{k}) + \xi^{y,xyy}(\mathbf{k}) - \xi^{x,yyy}(\mathbf{k}) + \xi^{y,xxx}(\mathbf{k}). \tag{A9}$$

These combinations correspond to the quantities represented in Fig. 3(b).